On Numerical Simulation of Flow Problems by Discontinuous Galerkin and Finite Volume Techniques

Ondřej Winter*[1], Petr Sváček[1]

[1]CTU in Prague, Faculty of Mechanical Engineering, Department of Technical Mathematics

Abstract

The paper deals with the comparison of numerical solutions of flow problems obtained by the discrete Galerkin method and finite volume method. The numerical solution calculated by the finite volume method was obtained using the open-source CFD package OpenFOAM and the numerical solution using the discontinuous Galerkin method was implemented using in-house code written in the Julia programming language.

Key-words: Finite Volume Method; Discontinuous Galerkin Method; OpenFOAM; Isentropic Volume; Forward Facing Step; Central/Central-Upwind schemes; HLL

1. Introduction

When one faces the problem of solving a partial differential equations by a numerical method, the following considerations need to be addressed appropriately: (i) in which way the solution $u(x,t)$ will be represented by an approximate numerical solution $u_h(x,t)$ and (ii) in which sense will the approximate solution $u_h(x,t)$ satisfy the partial differential equations, see [1]. There are other aspect of the numerical solution of partial differential equations such as the problem of domain discretization which is closely connected with the chosen approximation of the solution, see e.g. [2].

Common approach in the numerical simulations of the flow problems is to use the finite volume method based on the piecewise constant approximation of the solution in each cell. This method has many strong sides e.g. capability of solving problems on complex geometries, possibility of explicit semi-discrete form and easily achievable conservativity of the method, see e.g. [2]. On the other hand finite volume method has also some weak sides e.g. solution of the elliptic problems is challenging (can be overcome by special treatment, e.g. cell centred approach) and the fundamental problem of this method lies in the extension to higher-order accuracy, especially in case of the arbitrary grids, see e.g. [2, 1]. Furthermore, the theoretical analysis of higher-order finite volume method is not developed. Nowadays one is usually satisfied with hypothetical second order accuracy within cell centred approach with linear reconstruction supported by one of many limiters and/or filters, see e.g. [3] and references inside.

Natural solution to the accuracy problem is the finite element method which is based on globally connected local polynomial approximation on each element and provide us with the possibility to solve many problems on complex geometries, good formulation to solve elliptic problems, however from the global statement introduced by the globally defined basis and test functions destroys the locality of the scheme and may introduces problems with the solution of wave dominated problems see e.g. [1, 4], i.e., flow problems. The global statement also forbid the explicit semi-discrete formulation.

One might ask if by any sophisticated combination of the finite element and the finite volume methods could overcome the problems of both methods. Utilizing a space of basis and test functions like in the finite element method but satisfying the equations in a sense closer to the finite volume method, i.e., jumps at the boundary of the elements, appears to offer the method which has many of the desired properties. This combination leads to the discontinuous Galerkin method.

The discontinuous Galerkin method can be characterized as a method based on the idea of approximating the solution of a given problem by a piecewise polynomial function over a finite element mesh without any requirement on inter-element continuity [5]. This method do not solve all the problems of finite volume and finite element techniques and has some of the characteristics of these methods, e.g. higher modes of polynomial representation need to be filtered in case of appearing of strong gradients, see e.g. [1] and elliptic terms needs special attention, see e.g. [6, 7, 8]. On the other side local formulation permits explicit semi-discrete form, the method offers conservativity of the scheme and provides local high-order polynomial approximation. For recent know-how on the topic of discrete Galerkin method see e.g. [5] and references inside.

In this work, first the mathematical model, being the Euler's equations, is described. Next, brief description of one of the compressible fluid flow solver in free accessible open-source software OpenFOAM [9] without in-depth discussion of the finite volume discretization of space operators. Described solver *rhoCentralFoam* is based on central/central-upwind schemes of Kurganov and Tadmor, see [10, 11], generalized for arbitrary grids. Further, the discontinuous Galerkin method in nodal formulation is described together with numerical flux calculation (local Lax-Friedrichs and HLL fluxes). The implementation of the discontinuous Galerkin method was tested on isentropic vortex test case. Finally, the numerical results for more complicated problem are presented. The chosen case (forward facing step) is computed by finite volume and discontinuous Galerkin methods and these solutions are compared.

*Corresponding author: Ondrej.Winter@fs.cvut.cz

2. Mathematical Model

Consider the inviscid equations of gas dynamics, known as the Euler's equations, i.e., a set of three coupled nonlinear conservation laws, see [12], i.e.,

$$\frac{\partial \varrho}{\partial t} + \frac{\partial}{\partial x_j}(\varrho v_j) = 0, \tag{1}$$

$$\frac{\partial \varrho v_i}{\partial t} + \frac{\partial}{\partial x_j}(\varrho v_i v_j + p\delta_{ij}) = 0, \tag{2}$$

$$\frac{\partial \varrho e}{\partial t} + \frac{\partial}{\partial x_j}[(\varrho e + p)v_j] = 0, \tag{3}$$

where the conserved variables are density ϱ, momentum ϱv_i, and total energy ϱe, the fourth variable which is coupled using the constitutive equation with the system is the pressure p. The fluid is assumed to be ideal gas[1], i.e, the internal energy and the pressure are related through the equation of the state for the ideal gas. The total energy of the gas is the sum of the internal energy and kinetic energy, see e.g. [16], i.e.,

$$e = \varepsilon + \frac{v_k v_k}{2}, \tag{4}$$

where for the ideal gas the internal energy, see e.g. [17], reads

$$\varepsilon = c_v \vartheta, \tag{5}$$

where c_v is the specific heat at constant volume and ϑ is the thermodynamic temperature. The equation of the state can be written as

$$p = (\gamma - 1)\varrho\varepsilon. \tag{6}$$

The local speed of sound is then defined, see e.g. [18], as

$$c = \sqrt{\gamma \frac{p}{\varrho}}, \tag{7}$$

where γ is the adiabatic index, or alternatively as

$$c = \sqrt{(\gamma - 1)\left(h - \frac{v_k v_k}{2}\right)}, \tag{8}$$

where $h = e + \frac{p}{\varrho}$ is the enthalpy.

Finally, let us rewrite Euler's equations in the vector form, i.e.,

$$\frac{\partial \boldsymbol{q}}{\partial t} + \frac{\partial \boldsymbol{F}}{\partial x_1} + \frac{\partial \boldsymbol{G}}{\partial x_2} = 0, \tag{9}$$

where

$$\boldsymbol{q} = [\varrho, \varrho v_1, \varrho v_2, \varrho e]^T \tag{10}$$

is the state vector and

$$\boldsymbol{F} = \begin{bmatrix} \varrho v_1 \\ \varrho v_1^2 + p \\ \varrho v_1 v_2 \\ (\varrho e + p)v_1 \end{bmatrix}, \quad \boldsymbol{G} = \begin{bmatrix} \varrho v_2 \\ \varrho v_1 v_2 \\ \varrho v_2^2 + p \\ (\varrho e + p)v_2 \end{bmatrix} \tag{11}$$

are two nonlinear fluxes.

3. Finite Volume Model

In compressible fluid flows, the properties are both transported by the flow, and also propagated by the waves. This requires the construction of flux interpolations that take into account that transports can occur in any direction, see e.g. [19]. In presented finite volume method, the interpolations are from neighboring cells values to given face only, in this case the Kurganov and Tadmor approach can be used, see [10, 11].

Let us assume that computational domain Ω is approximated by polygonal domain Ω_h which consists of K control volumes V^k, i.e.,

$$\Omega \approx \Omega_h = \bigcup_{k=1}^{K} V^k \tag{12}$$

where V^k is an arbitrary polygon and boundary of the control volume ∂V^k consists of a set of the straight lines called the faces f. In finite volume technique, the local solution is interpreted as

$$\begin{aligned} \boldsymbol{x} \in V^k : u_h^k(\boldsymbol{x}, t) &= \bar{u}^k(t), \\ \bar{u}^k(t) &= \frac{1}{|V^k|}\int_{V^k} u_h(\boldsymbol{x}, t)\, dx, \end{aligned} \tag{13}$$

where for the sake of accuracy relining on linear reconstruction, the $\bar{u}^k(t)$ is located at the centroid $\boldsymbol{x}_k$ of the given control volume V^k. The semi-discrete form of the problem is formulated, i.e.,

$$|V^k|\frac{d\bar{\boldsymbol{q}}^k}{dt} = -\sum_f \boldsymbol{S}_f \cdot (\boldsymbol{F}_f, \boldsymbol{G}_f), \tag{14}$$

where $\sum_f$ denotes summation over all faces of the cell k and $_f$ denotes values at the face f and $\boldsymbol{S}_f$ is the outer normal with face area magnitude at the face f relative to the cell V^k.

The convective terms of the Euler's equations in tensor form are as follows

$$\boldsymbol{\nabla}\cdot(\varrho\boldsymbol{v}), \boldsymbol{\nabla}\cdot[(\varrho\boldsymbol{v})\otimes\boldsymbol{v} + p\boldsymbol{1}], \boldsymbol{\nabla}\cdot[(e\varrho)\boldsymbol{v}], \boldsymbol{\nabla}\cdot(p\boldsymbol{v}). \tag{15}$$

Each is integrated over a control volume and linearized, i.e.,

$$\int_V \boldsymbol{\nabla}\cdot(\boldsymbol{\Phi}\boldsymbol{v})\, dx \approx \sum_f (\boldsymbol{S}_f \cdot \boldsymbol{v}_f)\boldsymbol{\Phi}_f = \sum_f \phi_f \boldsymbol{\Phi}_f \tag{16}$$

where $\phi_f = \boldsymbol{S}_f \cdot \boldsymbol{v}_f$ is the volumetric flux, i.e. the volume of fluid flowing through the face per second. The numerical flux $\phi_f \boldsymbol{\Phi}_f$ is obtained by splitting in two directions, namely outgoing and incoming to the face of the cell, the following scheme is used

$$\phi_f \boldsymbol{\Phi}_f = \alpha\phi_f^+ \boldsymbol{\Phi}_f^+ + (1-\alpha)\phi_f^- \boldsymbol{\Phi}_f^- + \omega_f(\boldsymbol{\Phi}_f^- - \boldsymbol{\Phi}_f^+) \tag{17}$$

where $^+$ and $^-$ denote directions coinciding with the directions $+\boldsymbol{S}_f$ and $-\boldsymbol{S}_f$, respectively. Diffusive volumetric flux ω_f is based on the maximum speed of propagation of any discontinuity that may exist at a face between values interpolated in the $^+$ and $^-$ directions. Volumetric fluxes associated with the local speed of propagation are calculated as follows

$$\varphi_f^+ = \max(c_f^+|\boldsymbol{S}_f| + \phi_f^+, c_f^-|\boldsymbol{S}_f| + \phi_f^-, 0), \tag{18}$$

$$\varphi_f^- = \max(c_f^+|\boldsymbol{S}_f| - \phi_f^+, c_f^-|\boldsymbol{S}_f| - \phi_f^-, 0), \tag{19}$$

[1] Ideal gas with this definition is in some literature referred as calorically perfect gas, see [13, 14, 15].

where $c_f^{\pm} = \sqrt{\gamma \frac{p_f^{\pm}}{\varrho_f^{\pm}}}$. Diffusive volumetric flux ω_f is determined according to

$$\omega_f = \alpha(1-\alpha)(\varphi_f^+ + \varphi_f^-), \tag{20}$$

where weighting α is biased in the upwind direction, i.e.,

$$\alpha = \frac{\varphi_f^+}{\varphi_f^+ - \varphi_f^-}. \tag{21}$$

Evaluation of face values are done by the central scheme, except for the conserved variables, i.e., ϱ_f, $(\varrho \boldsymbol{v})_f$ and $(\varrho e)_f$ which are discretized by linear reconstruction with minmod limiter. The limiter is used on primitive variables $\boldsymbol{v}_f, \varrho_f, \vartheta_f$ to avoid unphysical negative values.

When the numerical fluxes are computed, the semi-discrete form of Euler's equation is integrated in time by explicit Euler method, i.e., the solution is represented in the time by finite difference approach.

4. Discontinuous Galerkin Method

In case of discontinuous Galerkin method, the computation domain Ω is also approximated by polygonal domain Ω_h which consists of K elements D^k, i.e.,

$$\Omega \approx \Omega_h = \bigcup_{k=1}^{K} D^k \tag{22}$$

where D^k is a straight sided triangle and ∂D^k is approximated by a polygon with each line segment being a face of a triangle. The solution $u(\boldsymbol{x}, t)$ is assumed to be approximated as

$$u(\boldsymbol{x},t) \approx u_h(\boldsymbol{x},t) = \bigoplus_{k=1}^{K} u_h^k(\boldsymbol{x},t) \in V_h = \bigoplus_{k=1}^{K} \left\{ \phi_n(D^k) \right\}_{n=1}^{N_p}. \tag{23}$$

Here $\{\phi_n(D^k)\}_{n=1}^{N_p}$ is a two-dimensional polynomial basis of order N defined on the elements D^k. The local solution is expressed as

$$\boldsymbol{x} \in D^k : u_h^k(\boldsymbol{x},t) = \sum_{i=1}^{N_p} u_h^k(\boldsymbol{x}_i^k, t)\ell_i^k(\boldsymbol{x}) = \sum_{n=1}^{N_p} \hat{u}_h^k(t)\psi_n(\boldsymbol{x}), \tag{24}$$

where $\ell_i(\boldsymbol{x})$ is the two-dimensional Lagrange polynomial defined by grid points $\boldsymbol{x}_n$ on the element D^k and u_h^k are nodal coefficients, i.e., grid point values in the element k, $\psi_n(\boldsymbol{x})$ is the local polynomial basis based on Jacobi's polynomials and $\hat{u}_h^k$ are modal coefficients. Modal representation is used to avoid problems with having to evaluate multidimensional integrals, see [1] and to easy evaluate the average values over elements which is needed for slope limiter. Order N is related to the N_p, i.e., number of the unknowns in the element, as

$$N_p = \frac{(N+1)(N+2)}{2}. \tag{25}$$

Let us introduce a mapping Ψ, connecting the general straight-sided triangle $\boldsymbol{x} \in D^k$, with the standard triangle, defined as

$$I = \{\boldsymbol{r} = (r,s) : r,s \geq -1; r+s \leq 0\}, \tag{26}$$

the connection of the two triangles I and D^k is done through assuming that D^k is spanned by the three vertices, $\boldsymbol{u}^1, \boldsymbol{u}^2, \boldsymbol{u}^3$ counted counter-clockwise, see Figure 1.

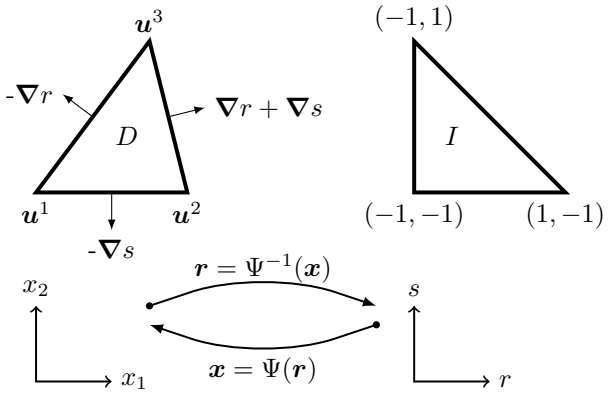

Figure 1. *Notation for the mapping between two triangles D and I.*

The mapping Ψ, i.e., direct mapping between element D^k and the standard triangle I, is defined as

$$\boldsymbol{x} = -\frac{s+r}{2}\boldsymbol{u}^1 + \frac{r+1}{2}\boldsymbol{u}^2 + \frac{s+1}{2}\boldsymbol{u}^3 = \Psi(\boldsymbol{r}). \tag{27}$$

Note that mapping is linear in $\boldsymbol{r}$, i.e., direct consequences of using elements with straight-edges, which means that Jacobian of the transformation is constant. The Jacobian J of the mapping Ψ reads

$$J = \frac{\partial x_1}{\partial r}\frac{\partial x_2}{\partial s} - \frac{\partial x_1}{\partial s}\frac{\partial x_2}{\partial s}. \tag{28}$$

In case of curvilinear edges, which are needed for preserving higher than second order accuracy for non-polygonal domains, the mapping Ψ is not linear in $\boldsymbol{r}$ and Jacobian differs in each curvilinear element.

For the local polynomial approximation the approximate solution u_h is rewritten as

$$\boldsymbol{r} \in I : u_h(\boldsymbol{r},t) = \sum_{i=1}^{N_p} u(\boldsymbol{r}_i,t)\ell_i(\boldsymbol{r}) = \sum_{n=1}^{N_p} \hat{u}_h(t)\psi_n(\boldsymbol{r}). \tag{29}$$

Equation (29) yields the expression, see [1],

$$\mathcal{V}\hat{\boldsymbol{u}} = \boldsymbol{u}, \quad \mathcal{V}^T\boldsymbol{\ell} = \boldsymbol{\psi}, \tag{30}$$

where $\hat{\boldsymbol{u}} = [\hat{u}_1, \ldots, \hat{u}_{N_p}]^T$ are the N_p modal coefficients and $\boldsymbol{u} = [u(\boldsymbol{r}_1), \ldots, u(\boldsymbol{r}_{N_p})]^T$ represents the N_p grid point values and $\mathcal{V}$ is the Vandermonde matrix. The Vandermonde matrix is defined as

$$\mathcal{V}_{ij} = \psi_j(\boldsymbol{r}_i). \tag{31}$$

Following the work of Hesthaven et al. [1], the basis $\{\psi_n(D^k)\}_{n=1}^{N_p}$ is chosen as

$$\begin{aligned}\psi_m(\boldsymbol{r}) = \sqrt{2}P_i^{(0,0)}(a)P_j^{(2i+1,0)}(b)(1-b)^i,\\ m = j + (N+1)i - \frac{i}{2}(i-1),\\ i,j \geq 0; \quad i+j \leq N,\\ a = 2\frac{1+r}{1-s} - 1; \quad b = s,\end{aligned} \tag{32}$$

where $P_n^{(\alpha,\beta)}(\cdot)$ is the n-th order Jacobi polynomial, for $\alpha = 0, \beta = 0$ the polynomial is reduced to Legendre polynomial. The process of finding locations of $\boldsymbol{r}_i$ for general order N described e.g. in [1] is computationally effective but little bit technical and the reader is left to look in the literature. The examples of locations of nodes for $N = 1, 2, 3$ are shown in Figure 2.

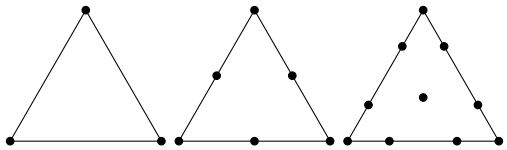

Figure 2. *Nodal sets on the equilateral triangle, from left* $N = 1, 2, 3$.

The weak formulation of Euler's equations, see e.g. [1], reads

$$\int_{D^k} \left(\frac{\partial \boldsymbol{q}_h}{\partial t}\phi_h - \boldsymbol{F}_h \frac{\partial \phi_h}{\partial x_1} - \boldsymbol{G}_h \frac{\partial \phi_h}{\partial x_2} \right) dx = \\ = \int_{\partial D^k} (n_1 \boldsymbol{F}_h + n_2 \boldsymbol{G}_h)^* \phi_h \, dx, \tag{33}$$

where $(n_1\boldsymbol{F}_h + n_2\boldsymbol{G}_h)^*$ is the numerical flux and n_1, n_2 are components of unit outer normal at ∂D^k. Test functions ϕ are chosen the same as the basis polynomials, i.e., Lagrange polynomials. To construct semi-discrete form, i.e.,

$$\mathcal{M}^k \frac{d}{dt}\boldsymbol{q}^k = \mathcal{S}_{x_1}^k \boldsymbol{F}^k + \mathcal{S}_{x_2}^k \boldsymbol{G}^k + \mathcal{F}^k(n_1\boldsymbol{F}^k + n_2\boldsymbol{G}^k), \tag{34}$$

where $\mathcal{M}^k$ is the mass matrix, $\mathcal{S}_{x_1}^k, \mathcal{S}_{x_2}^k$ are the stiff matrices for directions x_1, x_2, respectively and $\mathcal{F}^k$ is the flux mass matrix.

The mass matrix $\mathcal{M}^k$ is constructed as

$$\mathcal{M}_{ij}^k = \int_{D^k} \ell_i^k(\boldsymbol{x})\ell_j^k(\boldsymbol{x})\, dx = J^k \int_I \ell_i(\boldsymbol{r})\ell_j(\boldsymbol{r}), \tag{35}$$

since there is not known exact formula to compute the multidimensional integral of Lagrange polynomials, the substitution to modal formulation is done with aid of equation (30) and the alternative formula to compute mass matrix $\mathcal{M}^k$ is obtained, i.e.,

$$\mathcal{M}^k = J^k \mathcal{V}^{-T}\mathcal{V}^{-1}. \tag{36}$$

The evaluation of the stiffness matrices $\mathcal{S}_r, \mathcal{S}_s$ are constructed as follows. Using the chain rule, the differentiation with respect to x_1, x_2 reads

$$\begin{aligned}\frac{\partial}{\partial x_1} &= \frac{\partial s}{\partial x_1}\mathcal{D}_r + \frac{\partial s}{\partial x_1}\mathcal{D}_s,\\ \frac{\partial}{\partial x_2} &= \frac{\partial s}{\partial x_2}\mathcal{D}_r + \frac{\partial s}{\partial x_2}\mathcal{D}_s,\end{aligned} \tag{37}$$

where the metric constant $\partial(s,r)/\partial(x_1,x_2)$ are obtained from mapping Ψ. The differentiation matrices are computed by

$$\mathcal{D}_r = \mathcal{V}_r\mathcal{V}^{-1}, \quad \mathcal{D}_s = \mathcal{V}_s\mathcal{V}^{-1}, \tag{38}$$

where $\mathcal{V}_r, \mathcal{V}_s$ are defined as follows

$$\mathcal{V}_{r,(i,j)} = \left.\frac{\partial \psi_j}{\partial r}\right|_{\boldsymbol{r}_i}, \quad \mathcal{V}_{s,(i,j)} = \left.\frac{\partial \psi_j}{\partial s}\right|_{\boldsymbol{r}_i}. \tag{39}$$

Finally, the stiffness matrices are calculated, i.e.,

$$\mathcal{S}_r = \mathcal{M}\mathcal{D}_r, \quad \mathcal{S}_s = \mathcal{M}\mathcal{D}_s, \tag{40}$$

where $\mathcal{M}$ is mass matrix on I, i.e., $\mathcal{M}^k = J^k\mathcal{M}$, for in-depth discussion see e.g. [5, 1]. The remaining term is the surface integral over boundary of the elements, i.e.,

$$\int_{D^k} (n_1, n_2) \cdot (\boldsymbol{F}_h^k, \boldsymbol{G}_h^k)\ell_i^k(\boldsymbol{x})\, dx. \tag{41}$$

This integral is split into three egde/face components, i.e.,

$$\int_{D^{k,e}} \boldsymbol{n} \cdot (\boldsymbol{F}_h^k, \boldsymbol{G}_h^k)\ell_i^k(\boldsymbol{x})\, dx = \\ \sum_{j=1}^{N+1} \boldsymbol{n} \cdot (\boldsymbol{F}(\boldsymbol{x}_j), \boldsymbol{G}(\boldsymbol{x}_j)) \int_{\partial D^{k,e}} \ell_j^k(\boldsymbol{x})\ell_i^k(\boldsymbol{x})\, dx, \tag{42}$$

where $\boldsymbol{x}_j$ are locations of exactly $N+1$ nodal points along the edge and $\partial D^{k,e}$ is the edge $e = \{1, 2, 3\}$ of element k. This is advantage of the nodal representation over the modal representation, i.e., one only needs nodal values on the edge to evaluate integral (41). The flux mass matrix is contracted in the followings way, i.e.,

$$\mathcal{J}^k = \mathcal{V}\mathcal{V}^T\mathcal{E}^k, \tag{43}$$

where $\mathcal{E}^k$ is package of edge-mass matrices for individual edges of element, i.e.,

$$\mathcal{E}^k = \begin{bmatrix} J^{k,e}\mathcal{V}_1^{-T}V_1^{-1} \\ J^{k,e}\mathcal{V}_2^{-T}V_2^{-1} \\ J^{k,e}\mathcal{V}_3^{-T}V_3^{-1} \end{bmatrix}^T. \tag{44}$$

Here, $\mathcal{V}_e$ are one-dimensional Vandermonde matrices on the edges e and $J^{k,e}$ is Jacobian of the mapping between edge e of the element D^k and edge e of the standard triangle I.

For the computation of the numerical flux, the local Lax-Friedrichs flux is used, i.e.,

$$(n_1\boldsymbol{F}_h + n_2\boldsymbol{G}_h)^*_{\text{LxF}} = n_1\{\{\boldsymbol{F}_h\}\} + n_2\{\{\boldsymbol{G}_h\}\} + \\ + \frac{\lambda}{2}[\![\boldsymbol{q}_h]\!], \tag{45}$$

where

$$\lambda = \max_{s\in[\boldsymbol{q}^-,\boldsymbol{q}^+]} \left(|\boldsymbol{v}(s)| + \sqrt{\frac{p(s)}{\varrho(s)}} \right) \tag{46}$$

is an approximate local maximum of the wave speed. The terms $\{\{\cdot\}\}$ and $[\![\cdot]\!]$ are defined as follows

$$\{\{\boldsymbol{u}\}\} = \frac{\boldsymbol{u}^- + \boldsymbol{u}^+}{2}, \tag{47}$$

$$[\![\boldsymbol{u}]\!] = \boldsymbol{n}^-\cdot\boldsymbol{u}^- + \boldsymbol{n}^+\cdot\boldsymbol{u}^+. \tag{48}$$

Alternatively, the HLL (Harten-Lax-van Leer) flux is used, see [20], i.e.,

$$\boldsymbol{f}(\boldsymbol{u}^+,\boldsymbol{u}^-)^*_{\mathrm{HLL}} = \begin{cases} \boldsymbol{f}(\boldsymbol{u}^-), & s^- \geq 0, \\ \frac{s^+\boldsymbol{f}(\boldsymbol{u}^-) - s^-\boldsymbol{f}(\boldsymbol{u}^+) + s^+s^-(\boldsymbol{u}^+ - \boldsymbol{u}^-)}{s^+ - s^-}, & s^- \leq 0 \leq s^+, \\ \boldsymbol{f}(\boldsymbol{u}^+), & s^+ \leq 0, \end{cases} \tag{49}$$

where s^- and s^+ are estimates of the slowest and fastest wave speed, respectively, in the system. The estimates of these two speeds are as follows

$$\begin{aligned} s^- &= \min(|\boldsymbol{v}^-| - c, |\boldsymbol{v}^*| - c^*), \\ s^+ &= \max(|\boldsymbol{v}^+| + c, |\boldsymbol{v}^*| + c^*), \end{aligned} \tag{50}$$

where * variables are so-called Roe's averages, see [21], i.e.,

$$\begin{aligned} \varrho^* &= \sqrt{\varrho^-\varrho^+}, \\ \boldsymbol{v}^* &= \frac{\sqrt{\varrho^-}\boldsymbol{v}^- + \sqrt{\varrho^+}\boldsymbol{v}^+}{\sqrt{\varrho^-} + \sqrt{\varrho^+}}, \\ h^* &= \frac{\sqrt{\varrho^-}h^- + \sqrt{\varrho^+}h^+}{\sqrt{\varrho^-} + \sqrt{\varrho^+}}, \end{aligned} \tag{51}$$

and the speed of sound according to equation (8).

When is the right hand side of the semi-discrete equation (34) constructed, the equations are integrated in the time by explicit second order strong stability-preserving Runge-Kutta scheme. In each stage of Runge-Kutta scheme, the solution vectors $\boldsymbol{q}^k$ are limited with slope-limiter described in [1].

The implementation of described discontinuous Galerkin method is based on the MATLAB scripts available in [1] which were rewritten in to the Julia programming language [22].

5. Numerical Results

5.1. Isentropic Vortex

Let us first consider simple test case of isentropic vortex with known exact solution, see [23, 1], i.e.,

$$\begin{aligned} v_1 &= 1 - \beta e^{(1-r^2)}\frac{x_2 - x_2^0}{2\pi}, \\ v_2 &= \beta e^{(1-r^2)}\frac{x_1 - x_1^0}{2\pi}, \\ \vartheta &= 1 - \frac{(\gamma-1)\beta^2}{8\gamma\pi^2}e^{(1-r^2)}, \\ \varrho &= \vartheta^{\frac{1}{\gamma-1}}, \\ p &= \varrho^\gamma, \end{aligned} \tag{52}$$

where $r = \sqrt{(x_1 - t - x_1^0)^2 + (x_2 - x_2^0)^2}$, $x_1^0 = 5$, $x_2^0 = 0$, $\beta = 5$, and $\gamma = 1.4$. The problem is solved on the domain $\Omega_h = [0, 10] \times [-5, -5]$ for $t \in [0, 1]$. The exact solution is used as the initial condition and all boundary conditions are assumed to be cyclic in respective directions.

The numerical solutions were computed on three unstructured grids, i.e., $K = 228, 934, 4026$. Table 1 shows the accuracy of the scheme through the L^2-errors of the ϱe. The results were obtained with Lax-Friedrichs flux and shows very good convergence, see Figures 3 and 4 for illustration of rate of convergence on grid with $K = 228$ elements and examples of solutions for refined grids. Five contours of ϱ are shown.

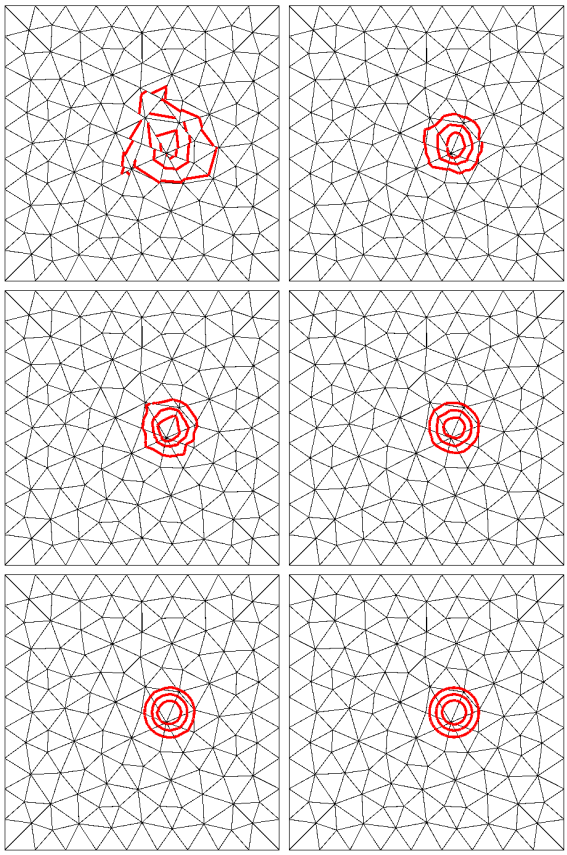

Figure 3. *Sequence of solutions to the isentropic vortex test case (with refined unstructured grids of size K = 228, 934, and 4026) using discontinuous Galerkin method with different order approximations. Five equally spaced ϱ contours are plotted. Top/Left: N=1, K=228; Top/Right: N=2, K=228; Middle/Left: N=3, K=228; Middle/Right: N=4, K=228; Bottom/Left: N=5, K=228; Bottom/Right: N=10, K=228.*

N	h	$h/2$	$h/4$	Rate
1	0.8332	0.2403	0.0430	1.58
2	0.2702	0.0404	0.0080	2.82
3	0.2154	0.0104	7.0758e−4	4.41
4	0.0529	0.0013	7.7671e−5	5.39
5	0.0380	4.0381e−4	7.2306e−6	6.56
10	0.0018	1.481e−7	1.5391e−9	13.58

Table 1. *Table of L^2 errors in ϱe for the isentropic vortex test case on a sequence of unstructured grids using different order approximations.*

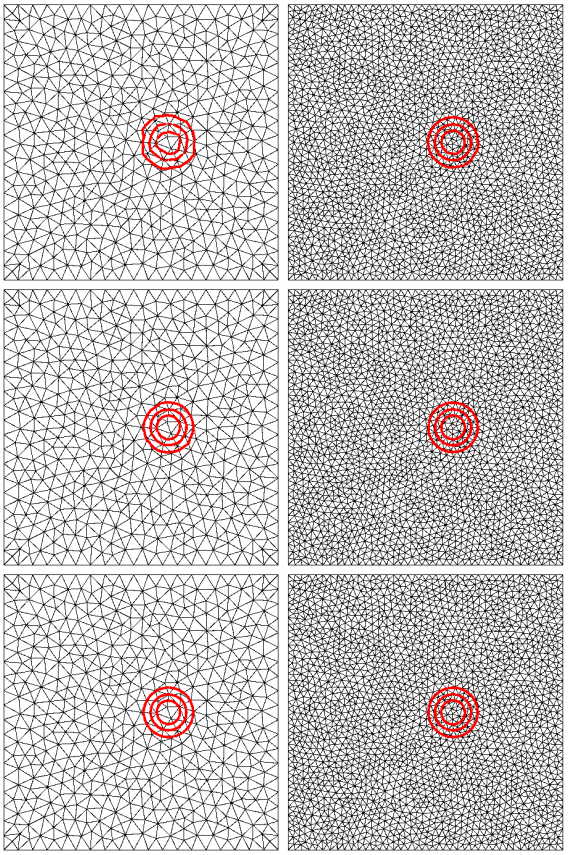

Figure 4. *Continuation of the Figure 3. Top/Left: N=1, K=934; Top/Right: N=1, K=4026; Middle/Left: N=2, K=934; Middle/Right: N=2, K=4026; Bottom/Left: N=3, K=934; Bottom/Right: N=3, K=4026.*

5.2. Forward Facing Step

Relatively challenging test case involving supersonic uniform flow encountering a forward facing step was chosen. This was originally studied in detail in [24] within finite volume framework and later in [25] in the context of discontinuous Galerkin. This case is very challenging and interesting because it generates unsteady solution with singularity in the solution and pressure singularity in time at the front of the step, see [24, 25, 1]. The computation domain is shown in Figure 5, the problem is computed for $t \in [0, 4]$.

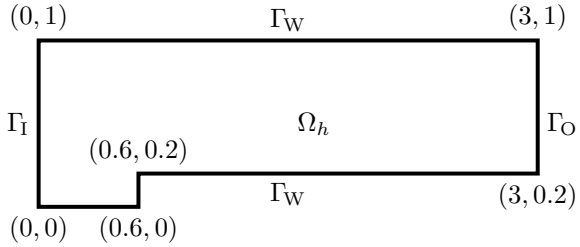

Figure 5. *Sketch of the domain in forward facing step case.*

The initial condition is a uniform flow given by

$$\varrho = \gamma, \ \varrho v_1 = 3\gamma, \ \varrho v_2 = 0, \ \varrho e = \frac{1}{\gamma - 1} + \frac{9\gamma}{2}, \quad (53)$$

where $\gamma = 1.4$. Boundary conditions are reflective at the wall boundaries. The inflow boundary condition is set to be the uniform Mach 3 flow, i.e., values given by initial condition and outflow is assumed to be supersonic, i.e, no boundary conditions are applied at the outflow.

Three successively, uniformly, refined grids are considered for finite volume method. Figure 6 shows ϱ contours of the solution at time $T = 4\,\mathrm{s}$. Direct comparison with results of [24, 25] shows good agreement.

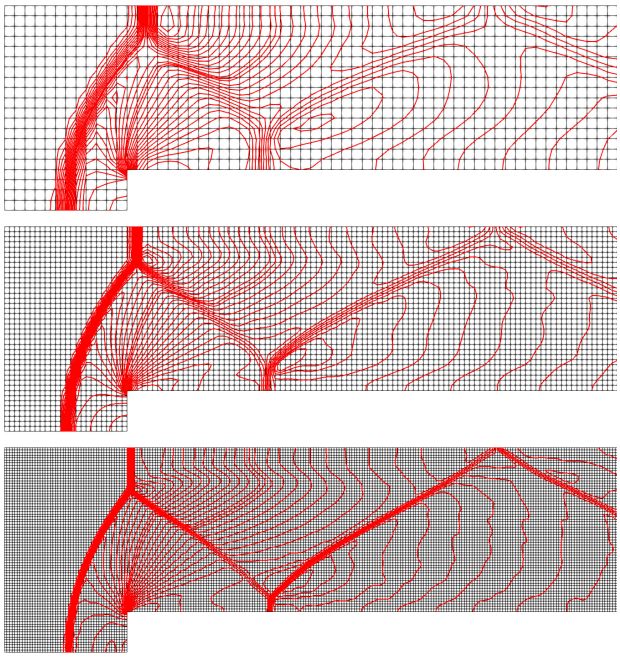

Figure 6. *Sequence of solutions to the Mach 3 forward facing step test case (with uniformly refined meshes of size K = 1008, 4032, and 16128) using the finite volume method. Thirty equally spaced ϱ contours are plotted.*

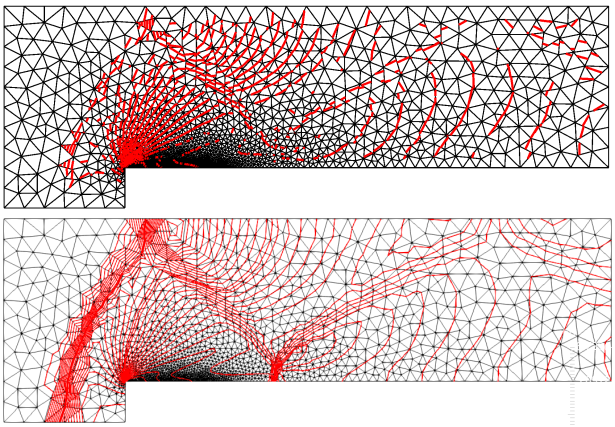

Figure 7. *Solution to the Mach 3 forward facing step test case solved with discontinuous Galerkin method N=1 for grid K=1549. Top: Solution is interpreted in discontinuous Galerkin sense. Bottom: Solution is interpreted in cell centered finite volume sense, i.e., elements averages are interpolated to the vertices. Thirty equally spaced ϱ contours are plotted.*

The numerical solutions obtained by discontinuous Galerkin method are shown on Figures 7, 8 and 9. The calculations were realized on three unstructured grids ($K = 1549, 5991, 17981$). The solutions show good agreement both with finite volume solutions and

with solutions in [25, 24]. The contours obtained from solution of discontinuous Galerkin method are visualized in two ways. First the solution is interpreted in discontinuous Galerkin sense and second the solution is interpreted as cell centred finite volume solution, i.e., elements averages are interpolated to vertices. The second method of visualization provides smooth contours, but essentially destroys the sharp resolution of shock waves. It is not clear how interpret the solution and this problem needs further investigation.

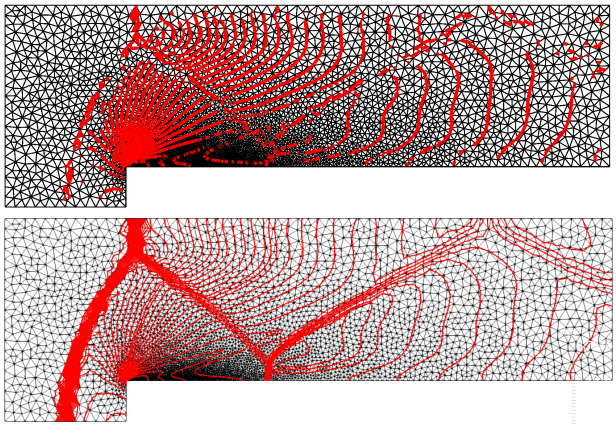

Figure 8. *Solution to the Mach 3 forward facing step test case solved with discontinuous Galerkin method N=1 for grid K=5991. Top: Solution is interpreted in discontinuous Galerkin sense. Bottom: Solution is interpreted in cell centered finite volume sense, i.e., elements averages are interpolated to the vertices. Thirty equally spaced ϱ contours are plotted.*

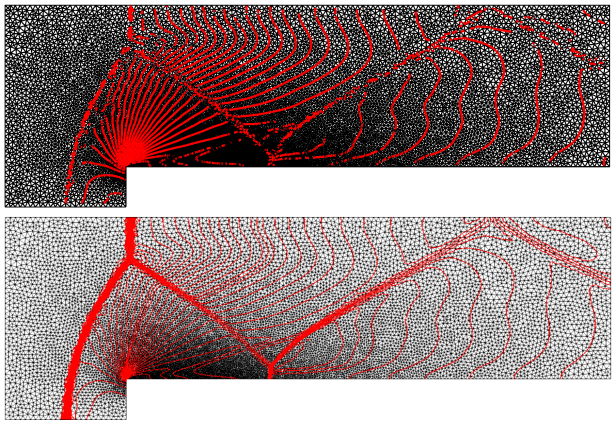

Figure 9. *Solution to the Mach 3 forward facing step test case solved with discontinuous Galerkin method N=1 for grid K=17981. Top: Solution is interpreted in discontinuous Galerkin sense. Bottom: Solution is interpreted in cell centered finite volume sense, i.e., elements averages are interpolated to the vertices. Thirty equally spaced ϱ contours are plotted.*

6. Conclusions

The central/central-upwind schemes of Kurganov and Tadmor implemented in OpenFOAM were described, then the construction of space operators of nodal discontinuous Galerkin method were covered. Further, the Julia language was proved to be effective way to do the numerical computing, i.e., MATLAB-like syntax is suited for rapid development and just in time compilation offers great performance (in many cases close to the C language), see [26, 27]. The convergence rate of implemented discontinuous Galerkin scheme was testes on isentropic vortex case and method shows very good behavior. Finally, the comparison of numerical solutions obtained by the Kurganov and Tadmor scheme and described discontinuous Galerkin method with HLL flux were done.

From the discontinuous nature of solution obtained with discontinuous Galerkin method it is not clear how visualize the data and this problem needs further investigation. Note also that in case of finite volume method the visualization is somehow cheating because the solution is interpreted as if it would be the finite element solution which results in e.g. smooth contours. This process however destroys the sharp resolution of the solution of the discontinuous Galerkin method.

Acknowledgement

This work was supported by the Grant Agency of the Czech Technical University in Prague, grant No. SGS16/206/OHK2/3T/12.

References

[1] J. S. Hesthaven and T. Warburton, *Nodal Discontinuous Galerkin Methods: Algorithms, Analysis, and Applications*. Springer, 2008.

[2] J. H. Ferziger and M. Perić, *Computational Methods for Fluid Dynamics*. Springer, third ed., 2002.

[3] R. J. LeVeque, *Finite Volume Methods for Hyperbolic Problems*. Cambridge University Press, 2002.

[4] O. C. Zienkiewicz, R. L. Taylor, and P. Nithiarasu, *The Finite Element Method for Fluid Dynamics*. Elsevier, seventh ed., 2014.

[5] V. Dolejší and M. Feistauer, *Discontinuous Galerkin Method: Analysis and Applications to Compressible Flow*, vol. 48 of *Springer Series in Computational Mathematics*. Springer, 2015.

[6] D. A. D. Pietro and A. Ern, *Mathematical Aspects of Discontinuous Galerkin Methods*. Springer, 2012.

[7] B. Rivière, *Discontinuous Galerkin Methods for Solving Elliptic and Parabolic Equations*. Society for Industrial and Applied Mathematics, 2008.

[8] G. Kanschat, *Discontinuous Galerkin Methods for Viscous Incompressible Flow*. Deutscher Universitätsverlag, 2007.

[9] H. G. Weller, G. Tabor, H. Jasak, and C. Fureby, "A Tensorial Approach to Computational Continuum Mechanics Using Object-Oriented Techniques," *Computers in Physics*, vol. 12, no. 6, pp. 620–631, 1998.

[10] A. Kurganov and E. Tadmor, "New High-Resolution Central Schemes for Nonlinear Conservation Laws and Convection-Diffusion Equations," *Journal of Computational Physics*, vol. 160, pp. 241–282, 2000.

[11] A. Kurganov, S. Noelle, and G. Petrova, "Semidiscrete Central-Upwind Schemes for Hyperbolic Conservation Laws and Hamilton-Jacobi Equations," *SIAM Journal on Scientific Computing*, vol. 23, no. 3, pp. 707–740, 2000.

[12] M. E. Gurtin, *An Introduction to Continuum Mechanics*, vol. 158 of *Mathematics in Science and Engineering*. Academic Press, 1981.

[13] R. B. Bird, W. E. Stewart, and E. N. Lightfoot, *Transport Phenomena*. Wiley, second ed., 2002.

[14] C. Truesdell and R. G. Muncaster, *Fundamentals of Maxwell's Kinetic Theory of a Simple Monatomic Gas: Treated as a Branch of Rational Mechanics*. Academic Press, 1980.

[15] C. Truesdell, *The Tragicomical History of Thermodynamics 1822–1854*. Springer, 1980.

[16] J. W. Gibbs, *Elementary Principles of Statistical Mechanics*. Scribner's sons, 1902.

[17] M. E. Gurtin, E. Fied, and L. Anand, *The Mechanics and Thermodynamics of Continua*. Cambridge University Press, 2010.

[18] A. H. Shapiro, *The Dynamics and Thermodynamics of Compressible Fluid Flow*, vol. I. The Ronald Press Company, 1953.

[19] R. J. LeVeque, *Numerical Methods for Conservation Laws*. Birkhäuser, second ed., 1992.

[20] A. Harten, P. D. Lax, and B. van Leer, "On Upstream Differencing and Godunov-Type Schemes for Hyperbolic Conservation Laws," *Society for Industrial and Applied Mathematics*, vol. 25, no. 1, pp. 35–61, 1983.

[21] P. L. Roe, "Approximate Riemann Solvers, Parameter Vectors, and Difference Schemes," *Journal of Computational Physics*, vol. 43, no. 2, pp. 357–372, 1981.

[22] J. Bezanson, A. Edelman, S. Karpinski, and V. B. Shah, "Julia: A Fresh Approach to Numerical Computing," *Society for Industrial and Applied Mathematics*, vol. 59, no. 1, pp. 65–98, 2017.

[23] H. C. Yee, N. D. Sandham, and M. J. Djomehri, "Low-Dissipative High-Order Shock-Capturing Methods Using Characteristic-Based Filters," *Journal of Computational Physics*, vol. 150, no. 1, pp. 199–238, 1999.

[24] P. Woodward and P. Colella, "The Numerical Simulation of Two-Dimensional Fluid Flow with Strong Shocks," *Journal of Computational Physics*, vol. 54, pp. 115–173, 1983.

[25] B. Cockburn, S.-Y. Lin, and C.-W. Shu, "TVB Runge-Kutta Local Projection Discontinuous Galerkin Finite Element Method for Conservation Laws III: One-Dimensional Systems," *Journal of Computational Physics*, vol. 84, pp. 90–113, 1989.

[26] A. Sengupta, *Julia High Performance*. Packt Publishing, 2016.

[27] J. Bezanson, S. Karpinski, V. Shah, and A. Edelman, "The Julia Language." https://julialang.org/. Accessed: 2018-03-30.